Age and Charge Effects in Cortical Bone: Raman Study of Phosphate Ions Stretching

Andrey Pavlychev[1], Xenia Brykalova[1], Aleksei Konashuk[1], Alexander A. Cherny[2] Anatoliy Korneev[3]

[1] St. Petersburg State University, Department of Physics, Peterhof, Saint Petersburg, Russian Federation;

[2] Vreden National Medical Research Center of Traumatology and Orthopaedics, Saint Petersburg, Russian Federation;

[3] St. Petersburg State University, Institute of Earth Sciences, Saint Petersburg, Russian Federation

Abstract

A quantitative assessment of internal electrostatic fields in bone tissue is conducted within the framework of the "bone-battery" concept. It is shown that their influence on the atomic structure and dynamics is significantly underestimated. To test this hypothesis Raman spectroscopy is applied to cortical bone of young and mature rats. Particular attention is paid to the $\nu_1(PO_4^{3-})$-band at 960 cm^{-1} in the Raman spectra to study the interference of P - O stretching with the dipole polarization of PO_4^{3-} ions in the electrostatic fields. The $\nu_1(PO_4^{3-})$-band is found split into the bulk and interface components with predominant Gaussian and Lorentzian shapes respectively. Their formation is a subject of site- and age-dependent dipoles polarization at the surface of nanocrystals. Based on the experimental and theoretical results, both the memory effect during the mineralization of bioapatite nanocrystals and quantum effects associated with low-dimensional quantization of valence states in hydrated nanolayers are predicted, and the prospects for the development of bone tissue engineering at the nanoscale are considered.

Keywords: native bone; aging phenomena; electrostatic fields; calcium carbonate hydroxyapatite; raman spectroscopy; atom-molecular architecture

1. Introduction

1.1 General remarks

Growing attention to biomineralization mechanisms [1-3] is motivated by their important role in the biosphere including the lithosphere, hydrosphere and atmosphere [4-6], in living organisms under physiogenic and pathogenic conditions and in the creation of biomimetic analogues [7-9]. The modern microscopic view on biomineralization is generally based on mineralogical and biomedical studies and relies primary on X-ray diffraction and electron microscopic investigations (see, e.g. [10, 11]). They show that the hard biological tissues form unique "organism-material" complexes [12-14], in which the dominant role is played by hexagonal calcium carbonate hydroxyapatite (HAP, $Ca_{10-x}(CO_3)_x(PO_4)_{6-x}(OH)_{2-x}$, $0 \leq x \leq 2$) with substantially variable stoichiometry that reflects the non-stationary conditions of their formation inside the voids of collagen fibers [15-19].

The variations in stoichiometry are conditioned by vacancies in the Ca^{2+} and OH^- positions and isomorphic substitutions in all crystallographic positions of HAP with concentrations dependent on peculiarity of biogenic surroundings. The views of different authors on the variations differ significantly [13-15,18-23]. In particular, the recent study of bio-chronological changes in bone [17] has revealed that deviations in stoichiometry are a source of specific charge heterogeneity in the mineral matrix. The interference of size, stoichiometric and charge effects results in the appearance of new structure-functional properties with intriguing mechanical and electrophysical characteristics, which stimulate further experimental and theoretical research in atomic structure and dynamics in native bone.

1.2 The bone-battery concept

The nanoscopic view of mineralized bone assembled from HAP nanocrystals (HAPNs) is presented in Fig. 1. The HAPNs inside a coplanar conglomerate are shown in the figure with shaded boxes separated one from the other by hydrated nanolayers. Since long order in HAPNs is broken, the electroneutrality condition valid for each individual unit cell in macro- and micro-crystals, is not longer applied to them. Thus, due to their small size, they are charged elements. To balance the charge distribution *Q(r)* the electroneutrality condition in bone can be rewritten in a more general form [17].

$$\int_S \frac{d}{dr} Q(\boldsymbol{r}) d\boldsymbol{r} \equiv 0. \qquad (1)$$

Integration region in Eq. (1) is a supercell *S* marked with white lines in Fig. 1.

Figure 1: Schematic presentation of a planar conglomerate of HAPNs (shaded boxes) separated one from other by hydrated nanolayers. Supercell *S* is shown with white lines.

The supercell *S* includes both a HAPN and the adjacent hydrated nanolayers. From Eq. 1 it follows that the excess of charge in a HAPN is compensated by opposite charges accumulated in the nanolayers. Charge alterations in mineralized bone are shown schematically in Fig. 2.

Comparative analysis of temporal changes in electron binding energies (BEs), lattice constants, calcium deficiency predicts an excess of negative charge accumulated in HAPNs [17]. The charge Q defined as a built-in charge, is maximum in newborn bone and drops with age. The relationship

$\Delta E_{core} = E^{HAP} - E^{bone} \approx$

$$-e\frac{Q}{4\pi\varepsilon_0}\left(\frac{1}{\varepsilon'<r'>} - \frac{1}{\varepsilon''<r''>}\right) > 0, \qquad (2)$$

links the built-in charge Q with the spectral shift ΔE_{core} of core-electron BE and allows the forecast of charge alterations. The charge Q is found equal approximately to ≈8 ±3 e^- and to ≈3 ±2 e^- in young and mature bone, respectively [17]. In Eq. (2)$< r' >$and $< r'' >$ are averaged distances up to vacant Ca^{2+} positions inside a nanocrystal and up to Ca^{2+} ions in the adjacent nanolayers; ε' and ε'' are the dielectric constants of bioapatite and intercrystalline environment, respectively.

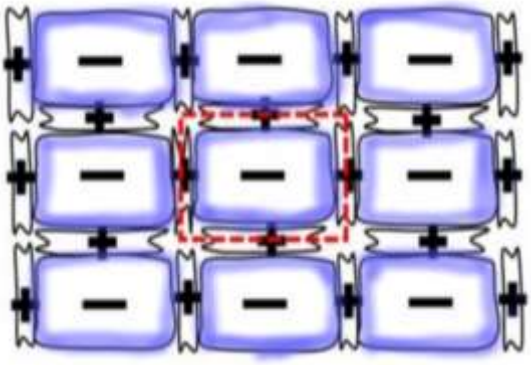

Figure 2: Schematic presentation of charges distribution in a coplanar HAPN conglomerate. Areas of strong changes in the electrostatic potential are highlighted in blue. Super(nano)cell is marked red.

The heterogeneity in charge distribution at the nanoscale allows us consider bone mineral as an electric battery consisting of a huge set of supercells, each of which is created by negatively charged HAPN immersed in a positively charged hydrated medium.

Using the extracted charges and sizes of HAPNs [17], the density P of electrostatic energy related with the charge inhomogeneity is estimated as $P > 10^6$ J/m^3 for young bone and $< 10^5$ J/m^3 for mature bone*. This estimation indicates the substantial decrease (more than 10 times) of the built-in energy $\mathscr{E}$ with age. This finding makes it evident that electrostatic field effects in bone are strongly underestimated. They can polarize atomic and molecular fragments, disturb ionic dynamics and bridge age with discharge phenomena in mineral bone.

1.3 Targets

The "bone-battery" (BB) concept opens up broad prospects for managing targeted drug delivery tailored to age and individual characteristics, creating new energy materials and developing new biomedical nanotechnologies that promote healthy and active longevity.

Our focus here is on the electrophysical phenomena related with electrostatic fields induced by built-in charges, and their impact on atomic dynamics in bone. The basic targets of the work are (i) to understand how strong and how distributed are the electrostatic fields; (ii) to quantify them and (iii) to trace back their role in aging phenomena.

Since the gradient of the electrostatic fields occurs especially strong on the contact of two neighboring nanocrystals (see, Fig. 2), the assembly of HAPNs can be approximately divided into two groups. The first one (A) is formed by atomic and molecular constituents of the bulk and the second group (B) consists of atoms and molecular fragments at the contact, where they are expected to be distorted by electrostatic forces more strongly than in the bulk.

The nanocrystal - hydrated nanolayer interface is conventionally regarded as a more disrupted region [21]. However, the electrostatic fields will favor for dipoles ordering of $[PO_4]^{3-}$, $[CO_3]^{2-}$ and $[OH]^-$ molecular ions, which is expected to be especially strong in young bone. To check this hypothesis our attention is on light scattering on valence electrons in respect with P-O stretching motion. This choice is motivated by the presence of narrow and intense $v_1[PO_4]^{3-}$-band at 960 cm^{-1} in the Raman spectra, which is almost universally accepted object of bone mineral content (see, e.g. [24-26]).

Considering the division of $[PO_4]^{3-}$ ions into the bulk and interface moieties the splitting of $v_1[PO_4]^{3-}$-band into two components in the Raman spectra of native bone can be reasonably predicted. One of the subbands (*A*) associated with the first group, is expected to show similarity to the $v_1[PO_4]^{3-}$-band in HAP, whereas the second subband (*B*) will be noticeably shifted downwards and distorted by the electrostatic fields at the contact.

On this background the main objectives are (i) to detect and document the splitting of the $v_1[PO_4]^{3-}$ Raman bands in young and mature bone and (ii) to compare their performance with that forecaster within the BB concept. The methods of sample preparation and the Raman band analysis are described in Section 2. Section 3 evaluates the electrostatic fields in bone and presents the results of the analysis of the experimental spectra. In Section 4, it is shown that Raman probing provides us with additional evidence indicating the relationship between buil-in charges and age-related changes in bone tissue, which was predicted based on the analysis of XRD and XPS data [17, 27].

2. Materials and Methods

2.1 Samples

The bone samples were prepared ex-situ on air from cortical layers of middle third (diaphysis) of the femur, tibia and humerus white mongrel young and mature, male rats weighting respectively 40 – 60 g (n = 8) and 250 – 280 g (n = 6).

All experimental procedures involving animals were performed in accordance with the ARRIVE guidelines. The research complies with all applicable national laws (GOST R ISO 10993-2-2009 − medical devices, biological evaluation of medical devices; part2, animal welfare requirements), regulations and guidelines in accordance with ISO 10993 that ensures the high animal welfare standards, as well as national regulations rules GOST 33215-2014 and GOST 33216-2014 − rules for the maintenance and care of laboratory rodents and rabbits. The study protocol 10-10-2015 was approved after reviewing by Local Ethic Committee of R.R. Vreden National Medical Research Centre of Traumatology and Orthopaedics. All animals were kept under identical conditions in the vivarium of the National Medical Research Center of Traumatology and Orthopedics.

Cortex was thoroughly cleaned of soft tissue, washed in saline, dried with blotting paper, and grinded to fine powder with particles of size ~ 1 mm. This sample preparation does not affect the measured spectra. No heating of the bone samples was used. To document the HAP-to-bone distortions the HAP crystal in almost stoichiometric composition synthesized as it is described in [22, 28] is used as a reference compound.

The structural parameters of the samples determined by using the X-ray diffraction (XRD) [17,27], are collected in Table 1. In addition to the HAP lattice constants $a = b$ and c, mean linear

sizes <*L*> and degrees *D* of crystallinity of HAPNs, mean thickness <*d*> of nanolayers, effective numbers *N* of atoms per a HAPN, the charges *Q* in young an mature bone as well as the expected errors are exhibited in the table.

Table 1: Structural and charge parameters of the atom-molecular architecture of young and mature bone samples. Structural parameters *a*, *c*, <*L*> and <*d*> are given in Å, charge *Q* is in e^- and *N* is the averaged number of atoms per NHAP).

Parameters	**Young bone**	**Mature bone**
a	9.413±0.001	9.396±0.001
c	6.849±0.001	6.875±0.001
<*L*>	35±5	45±5
<*d*>	12±2	7.5±2
D %	84±4	96±4
N	1800±500	3800±500
Q	8±5	3±2

2.2 Raman probing

Raman techniques (see, e.g. [26]) provides not only basic phase identification in complex materials but, examining subtle changes in light scattering, fine effects at the nanoscale can also be assessed. This method is a unique tool for probing and mapping nanophases dispersed in matrices (see, e.g., [29,30]), surface nanophases [31], charge transportation [32, 33], film orientation [34], clusters size [35], configurational order [36], interfacial reactions [37], and mechanical loads [38]. This spectroscopy is used here to study site-dependent interference of “mechanical” and “electrical”

properties associated with P --O stretching and dipole polarization of $[PO_4]^{3-}$ ions in young and mature bone.

Static disordering and dynamic dephasing are two extreme mechanisms leading respectively to the Gaussian and Lorentzian broadening of Raman signals (see, e.g. [39]). Our attention is drawn to specific changes in the shape of the Raman signals. We expect, first, to detect a two-component $v_1[PO_4]^{3-}$-band structure, the analysis of which allows us to quantify the different impact of electric fields on the bulk and interface components and, second, to check their compliance with the BB expectations. It is supposed that $[PO_4]^{3-}$ ions in the contact region undergo both static disordering and polarization along the strength lines. Hence the Lorentzian shape of the subband *B* will be more pronounced, the higher the consistency of P-O stretching in the corresponding regions.

This expectation motivates the choice of Voigt functions to approximate the experimental bands. It allows for the direct extraction of the Gaussian and Lorentzian widths W_G and W_L, which are considered markers of static disorder and coherence of excited $[PO_4]^{3-}$ fragments responsible for the formation of the subbands *A* and *B*.

The analysis of the fitting procedure shows that the choice of two functions is optimal for modeling the $v_1[PO_4]^{3-}$-band in the bone specimens. Then, to document the bandshapes in young and mature bone, we postulate the use of two Voigt functions whose positions and Gaussian and Lorentzian widths are not fixed in advance and are determined based on the best fitting for the experiment. With this approach, comparing the extracted widths with those expected within the BB concept allows for a quantitative characterization of its applicability. In addition to widths, analysis of changes in the relative intensities of the subbands and their Raman shifts in young and mature bone is also used to test the concept.

3. Results

3.1 Experimental

Raman measurements of the bone samples and the reference HAP crystal were performed in the wide spectral interval (300 −4000 cm^{-1} and, then, in more detail in the narrow interval 920 −990 cm^{-1} by using the Raman spectrometer Horiba Jobin-Yvon LabRam HR800 ((the Science Park of Saint Petersburg State University, projects 101-22060, 112-22072, 113-22068, 119-13853) and the Olympus BX 41 microscope (40x objective) with green laser (532 nm) excitation, see for detail [40]. (Prof. E. Rühl' laboratory, Freie University, Berlin, GRISC-projects P-2017b-1, P2018b-12). The Raman spectra of bone samples recorded several times have demonstrated a good reproducibility. No samples charging or decomposition effects were detected.

The measured spectra of young and mature bone and HAP in the narrow interval are shown in Fig. 3. The smooth background determined from wide-range Raman measurements has been subtracted in the figure. The intense $v_1(PO_4^{3-})$-band in bone is substantially broadened and asymmetric compared to that in HAP crystal. The broadening is not surprising effect because the crystalline structure in mineral bone is more disordered than that in HAP, but the band asymmetry and its documentation need further investigations.

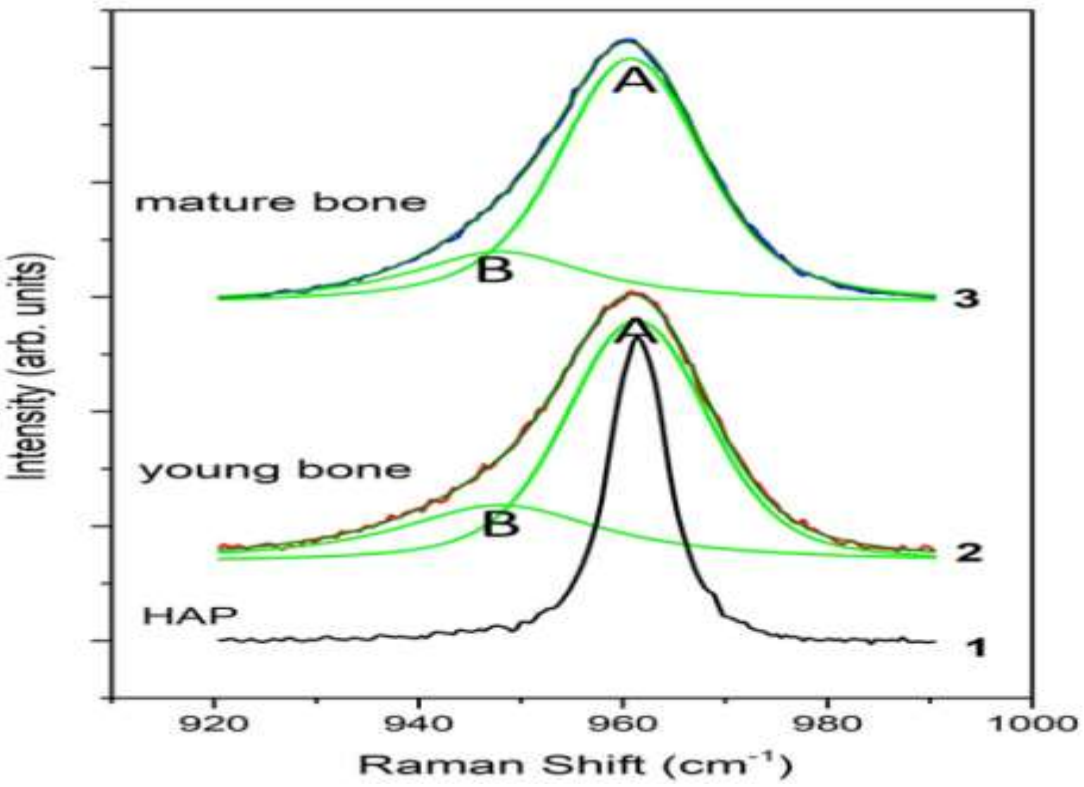

Figure 3: Experimental Raman spectra in the narrow interval 920 - 990 cm^{-1}. The measured $v_1[PO_4^{3-}]$-band in young and mature bone (symbols); the band fits (thin lines). The extracted *A* and *B* components are shown with green lines. The $v_1[PO_4^{3-}]$ band in HAP is also exhibited.

3.2 Assessment of electrostatic effects

To assess the electrostatic fields, the concept of double electrical layers (DELs) is used. The DEL effect in bone was previously reported by Wilson and co-authors in the work [41]. By examining the NMR spectra they have assigned it with $[PO_4]^{3-}$ ions on the surface of HAPNs and their charge compensation by Ca^{2+} ions accumulated in the hydrated nanolayers.

Another origin of DELs follows from the BB concept: the negative charged layers arise not so much from broken phosphate bonds on the surface but from the built-in charge *Q*. Considering high mobility of hydroxide anions in HAP one may suppose that they squeezed out of the bulk by

intrinsic electrostatic repulsive forces, accumulate at surfaces of HAPNs. Thus, the charge Q_{surf} is associated not so much with $[PO_4]^{3-}$ as with the excess $[OH]^-$. We assume $Q_{surf} \geq Q$ and the contribution of phosphate ions is not significant because of surface relaxation in HAPN.

In the contact region of two HAPNs the electrostatic fields can be approximately described by combining two mirror-symmetric DELs. Fig. 4 illustrates this model: left and right DELs correspond to the left and right ends of two neighboring HAPNs. Black and white triangles, as well as white and green hexagons refer respectively to hydroxides, hydroxide vacancies, Ca^{2+} vacancies and $Ca^{2+}(H_2O)_n$ clusters.

As a next step, the DELs are described as flat capacitors: $(^-||^+)$ and $(^+||^-)$, the negative $^-|$ (red) and positive $|^+$ (green in Fig. 4) plates of which are charged by $[OH]^-$ anions pushed to the surface and Ca^{2+} cations compensating the total charge. This simple model makes it clear that hydrated nanolayers in bone represent potential wells $\varphi(x)$.

Assuming $L >> \frac{1}{2}d$, uniform distribution of Q_{surf}, linear dependence of electric field strength $\boldsymbol{F}$ in the capacitors and neglecting edge effects in them, we derive $\varphi(x)$ is a V-shaped potential well. In the interval $-\frac{1}{2}d \leq x \leq +\frac{1}{2}d$ it is

$$\varphi\vee(x) = \frac{2\Delta\varphi}{d}|x|, \qquad (3)$$

where $\Delta\varphi$ is the potential difference:

$$\Delta\varphi \approx \frac{Q_{yz}}{C_{yz}}, \qquad (4)$$

between the $^-|$ and $|^+$ charged plates. Q_{yz} is a part of Q_{surf} falling on a yz-plate (see, Fig. 4) and the capacity C_{yz} is

$$C_{yz} = \frac{2\varepsilon''\varepsilon_0}{d} S_{yz}, \qquad (5)$$

where S_{yz} is the surface of the plate. The total capacity of a single HAPN is $C=\sum_{j,j\neq i} C_{ij}$. The directions of $\boldsymbol{F}$ are marked in Fig. 4.

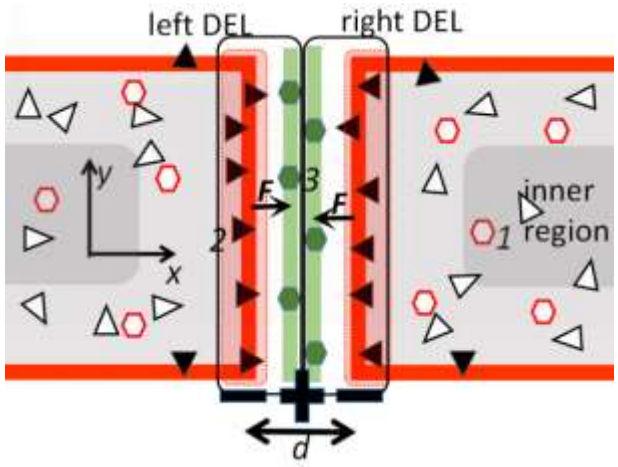

Figure 4: Schematic presentation of contact region between two neighboring nanocrystals in bone; the solid red and green stripes refer to negatively and positively charged nanolayers of two DELs (see text). Black and white triangles refer to OH^- on the surface and OH^- vacancies in the bulk; white and green hexagons refer to Ca^{2+} vacancies and $Ca^{2+}(H_2O)_n$ clusters in hydrated layers, respectively. The inner region (see text) of HAPNs is darkened.

Using the sizes and charges in Table 1, neglecting age variations of ε' and ε'', considering that HAPNs in the bone samples are elongated along the *c* (|| z) axis by about 5 (- 6) times more than along the *x* and *y* axes and applying Eqs. 3 and 5, the potential difference and the electrostatic field strength are estimated as $\Delta\varphi^{young} \approx 140 \pm 50$ mV and $\boldsymbol{F}^{young} \approx 230 \pm 80$ kV/mm for young bone, respectively. In mature bone the characteristics are reduced by more than an order of magnitude, reaching values of $\Delta\varphi^{mature} \approx 10$ mV and $\boldsymbol{F}^{mature} \approx 25$ kV/mm. Thus, we infer that with age the potential well in the contact region becomes narrower and much shallower.

Figure 5 shows the potentials $\varphi(r)$ for young and mature bone over a wider range. For their

comparison, it is assumed that $\varphi(r) \approx 0$ in the inner region of HAPN (see Figs. 4 and 5), since due to the high mobility of hydroxide, the Coulomb potentials created by both Ca^{2+} and OH^- vacancies compensate each other. Taking into account the charge distributions, the potential can be represented as:

$$\varphi(r) = \begin{cases} \frac{2\Delta\varphi}{d}|r| - V_0, & \text{for } -\frac{1}{2}d \le r \le +\frac{1}{2}d \\ e^{-\alpha r}, \text{for } r \in (\pm\frac{1}{2}d, \pm\frac{1}{2}(b)) \end{cases}. \qquad (6)$$

Inside hydrated nanolayers the $\varphi(r)$ is a V-shaped potential well of depth V_0. Potential barriers are formed on the surface of HAPNs, and inside them the potential $\varphi(r)$ decreases exponentially. b (= d+L) is the mean size of the supercell S and α determines the rate of decrease of potential. The potential in Fig. 5 is obviously smoothed out due to the finite dimensions of the charge distribution and atomic motions.

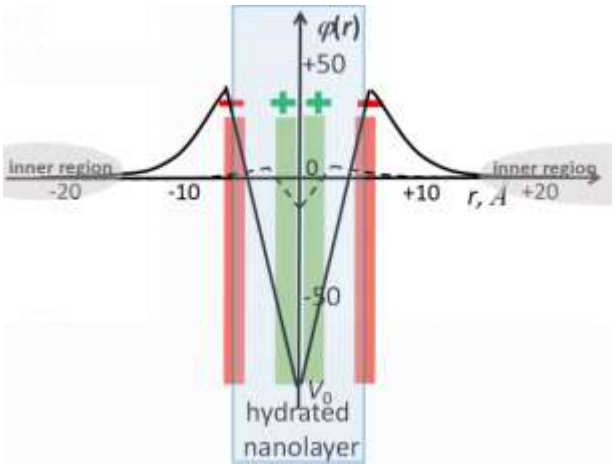

Figure 5: Schematic presentation of the potential $\varphi(r)$ in young (solid line) and mature bone (dash line). Hydrated nanolayers in shown with light blue.

The assessments of electrostatic fields confirms the predicticted (Sect. 1.3) changes in atomic

dynamics in bone. Thus in addition to static disorder, the interface will also be characterized by an alignment of dipoles along the direction of the electrical forces. As a result a more pronounced Lorentzian shape of the subband *B* compared to the subband *A* in the Raman spectra of bone is suggected.

3.3 Data analysis

To test these assessments, the measured $v_1(PO_4^{3-})$-bands in young and mature bone are examined in more details. The best Voigt fit results are plotted with solid black lines in Fig. 3. The extracted Raman shifts $E_{A(B)}$, Lorentzian (W_L) and Gaussian (W_G) full-widths-at-half-maximum of the subbands *A* and *B* as well as the relative intensity $\frac{B}{A+B}$ are collected in Table 2. The spectroscopic parameters of the $v_1[PO_4]^{3-}$-band in HAP are shown too. The coefficients χ^2 are also given in Table 2. Since the spectral positions, Gaussian and Lorentzian widths were not fixed in advance the extracted parameters are regarded as independent characteristics of the subbands.

Table 2: Spectroscopic parameters of mineralized bone: Raman shifts $E_{A(B)}$, Lorentzian (W_L) and Gaussian (W_G) FWHM of the *A* and *B* components for newborn and mature bone. In HAP, only one Voigt function was used for fitting. The parameters are averaged over all bone samples.

Spectrosc. parameters	HAP	Young bone		Mature bone	
		A	B	A	B
E in cm^{-1}	961.4 ±0.2	961.3 ±0.5	948 ±0.5	960.7 ±0.5	948 ±0.5
W_L in cm^{-1}	4.7±0.2	6±1	13±1	8.5±1	21.5±1
W_G in cm^{-1}	3.7±0.2	24±1	3±1	11.5±1	2±1

Ratio $\frac{B}{A+B}$,	0	0.31±0.05	0.24±0.05
Ratio $\frac{L}{G}$	1.3±0.1	0.5±0.1	1.3±0.1
Coeff χ^2	435	500	290

The spectroscopic parameters in Table 2 make evident the resemblance of the position of the intense high-frequency subband *A* with the $\nu_1[PO_4]^{3-}$-band in HAP crystal. The subband *A* appears as a pronounced Gaussian ($W_G^A >> W_L^A$). One may see in Table 1 that the width W_G^A narrows more than twofold with age, which is qualitatively consistent with the increase in the degree of crystallinity in mature bone compared to young bone. As for the Lorentzian width W_L^A it varies weaker and is much smaller than W_G^A. Thus, the similarity of the Raman shifts of the subband *A* with the $\nu_1[PO_4]^{3-}$-band in HAP crystal and its Gaussian shape allows us to assign the subband *A* with the $[PO_4]^{3-}$ moieties in the bulk.

The subbands *B* in the spectra of both young and mature bone are shift downward by 13.3 and 12.7 cm^{-1} compared to the $\nu_1[PO_4]^{3-}$-band in HAP. This significant shift is an indicator of the link of the subband with $[PO_4]^{3-}$ moieties at the interface.

In line with our expectations, the extracted shapes of the subbands A and B show significant differences. The *B* is a distinct Lorentzian ($W_G^B << W_L^B$) whereas the *A* is a Gaussian in the Raman spectra of both young and mature bone. This difference is, firstly, a marker of strong static disordering of HAPN, especially in young bone, and, secondly, of strong polarization of P-O dipoles in the contact region.

In addition to the distinctions in shape, Table 2 demonstrates (i) a minor but distinct downward displacement Δ_A of the subband *A*: E_A(mature) ≈ 960.7 cm^{-1} < E_A(young) ≈ 961.3 cm^{-1}, and (ii) a

decrease in the contribution of the subband *B* to the total signal with age:

$\frac{B}{A+B}$(mature) < $\frac{B}{A+B}$(young). (7)

4. Discussion

4.1 Electrostatic effects

An assessment of the electrostatic fields generated by embedded charges, obtained within the framework of the BB concept, shows that ion polarization on interface and in hydrated nanolayers cannot be ignored. The results of the Raman study of symmetric P–O vibrations in young and mature bone are consistent with this assessment.

However, it should be noted that the estimates of $\Delta\varphi$ and $\boldsymbol{F}$ were made using multiple approximations. Ca^{2+} vacancies in HAPN are assumed to be uniformly distributed, and the dielectric constants ε' and ε'' are regarded as to be close to those of imperfect HAP crystals [42] and water [17] (≈15 and ≈80, respectively). These values do not take into account (i) the constant ε'' is a subject of substantial variations in dependence of distance to the surface of HAPN [43], (ii) the morphology of the interfaces and (iii) the acceleration of molecular motions in external potentials [44, 45] and (iv) the constant ε' depends on the specific imperfections in bioapatite. Besides, the condition $L>>{}^{d}/_{2}$ assumed by Eqs. 4 and 5, requires further investigations as applied to nanoelements. The finite dimension of charge distribution on $^{-}|$ and $|^{+}$ plates are completely ignored.

Since the contribution of $[PO_4]^{3-}$ ions to Q_{surf} was not taken into account, the both potential difference and electrostatic strength are somewhat underestimated. Hence the electric fields may be stronger than predicted here.

High polarization and ordering of PO_4^{3-} at the interface is a rather unexpected result, as a more common view is a significant structural disorder there (see e.g. [21]). Although it does not mean restoring of the crystalline structure, but it does indicate its substantial structural deviations from amorphous calcium phosphate [46].

To clarify the feature, let us compare Raman signals coming from bone tissues and the exoskeleton of invertebrates. Raman spectra of the exoskeleton provide successful probing of CO_3^{2-} ions in various surroundings [47] as $CaCO_3$ polymorphs form the mineral phase of invertebrates. The studies of the $v_1[CO_3^{2-}]$-band shapes face with similar difficulties in understanding their asymmetry compared to the band in the reference spectra of calcium carbonates. According to Wehrmeister et al. [47] the $v_1[CO_3^{2-}]$-band is composed from two components: the high-frequency Lorentzian at 1088 cm^{-1} and the low-frequency Gaussian at 1078 cm^{-1}. They correspond respectively to nanocrystalline $CaCO_3$ and amorphous calcium carbonate phases. In particular, the composition was detected in palm of the Callinectes Sapidus crab claw and the Calappa granulata exoskeleton [48, 49].

Examining the Raman $v_1[CO_3^{2-}]$-band in combination with the Ca 2p NEXAFS spectroscopic and electron microscopic data, Katsikini and co-authors [48] have confirmed the assignment of the Lorentzian and Gaussian subbands with $CaCO_3$ crystalline and amorphous phases and linked their intensities with the site-dependent changes in the crystallinity of the exoskeleton.

At first glance, the two-component layout of the $v_1[PO_4^{3-}]$ and $v_1[CO_3^{2-}]$ bands appears to be a marker of their similar origination. However, the permutation of the Gaussian and Lorentzian components in the bands indicates their significantly different nature. To investigate the difference it could be assumed that the $v_1[PO_4^{3-}]$-band has the similar crystalline-amorphous origin too. Pay

attention that this assumption is supported by the Raman studies of amorphous calcium phosphates [50, 51], according to which the $\nu_1[PO_4]^{3-}$ band in them is observed at 10 - 13 cm^{-1} lower than the band in the HAP crystal, that is, with the same Raman shift where subband B is located.

To test the crystalline-amorphous genesis of the $\nu_1[PO_4^{3-}]$ band asymmetry, we postulated the Lorentzian and Gaussian shapes of its high- and low-frequency components and found that the best fitting criterion $\chi^2 \approx 1817$ is almost 8 times worse than the fitting results in Fig. 3. This decline does not certainly mean that the mixing of crystalline and amorphous phases does not play any role in shaping the $\nu_1[PO_4]^{3-}$-bands in bone, but it does indicate that there are other and more significant mechanisms controlling their appearance. One of these is the dipole polarization of $[PO_4]^{3-}$ ions and their ordering in the intrinsic electrostatic fields in bones. Thus, the results do not support the common view that the low-frequency shoulder is due to amorphous mineral; instead it reflects ordered but distorted $[PO_4]^{3-}$ groups at the interface under strong electric fields.

Despite the smallness of the displacement Δ_A reported in Sect. 3.3, we draw attention to it, since its sign serves as additional confirmation of the hypothesis about the influence of electrostatic fields on atomic dynamics. The Δ_A cannot be rationalized in terms of an adiabatic compression of PO_4^{3-} ions as the HAP unit cell is found less compressed in young bone than that in mature one [28]. On the contrary, an upward displacement would be expected. That is why to explain it our emphasize is on the electrostatic interactions, namely, on Coulomb repulsion between anions inside HAPN. As $|Q(\text{mature})| < |Q(\text{young})|$, the frequency ω of P -- O stretching decreases with age resulting in $E_A(\text{young}) > E_A(\text{mature})$. Hence the sign of Δ_A is an indicator of charge Q dissipation with age.

The weakening of electrostatic fields and the growth of HAPN with age are qualitatively consistent

with inequality (7). However, the observed decrease in the relative intensity $\frac{B}{A+B}$ is significantly less than expected due to the extracted changes in charge and size (see, Table 2). One may assume that this discrepancy is associated with the preservation of the direction of dipoles in young bone during the deposition of the upper atomic layers as the HAPNs grow, that is, one can talk about the memory of dipoles direction as the bone ages.

Further confirmation of the memory effect can be obtained by analyzing the cumulative changes in the Lorentzian and Gaussian contributions to the $v_1[PO_4^{3-}]$-band with age. Let us introduce the coefficient $\frac{L}{G}$ as

$$\frac{L}{G} = \frac{W_A^L \frac{A}{A+B} + W_B^L \frac{B}{A+B}}{W_B^G \frac{A}{A+B} + W_B^G \frac{B}{A+B}}. \qquad (8)$$

It shows the ratio of the Lorentzian and Gaussian distributions to the band. The coefficients $\frac{L}{G}$ computed for young and mature bone and the HAP crystal using Eq. (8), are given in Table 2. It is seen that the Lorentzian part is minimum in young bone and, although static disorder decreases with age, the coefficient $\frac{L}{G}$ increases and, in the case of mature bone, approaches the value characteristic of the HAP crystal. This result further confirms the applicability of the chosen method of $v_1[PO_4]^{3-}$bandshape analysis using Voigt functions.

4.2 Prospects

The assessment of electrostatic fields in mineral bone shows (i) their important role in the interface of HAPNs and (ii) their significant decrease with age. It should be noted that the decrease is quite dramatic, because the expected potential difference $\Delta\varphi$ for young bone noticeably exceeds the kinetic energy ($k_B T$) of the thermal motion of atoms, whereas in mature bone the difference $\Delta\varphi$ is

virtually smoothed out by the thermal movements. We also note that the $\Delta\varphi$ in young bone exceeds the membrane potential (70 - 90 mV), but is much smaller in mature bone.

The predicted potential $\varphi(r)$ variations allow us to expect the occurrence of such quantum phenomena as electron trapping within the potential wells and electron tunneling through the potential barriers (see Fig. 5) as they propagate through the mineral bone. Indeed, to quantify the valence band structure of bone, the three-dimensional superlattice (3DSL) model was proposed in the work [52]. The model relates the valence band energy in bone to the electron-optical properties of the supercell S using the relation

$$e^{2ikb_j} - 2Re\left(\frac{1}{T(E)}\right)e^{ikb_j}+1=0. \qquad (9)$$

It links the certain electron energy E with the vector $\boldsymbol{k}$ in the superperiodic potential of a conglomerate, where T is the amplitude of electron transmission through the supercell S, b_j is the mean size of S in the direction j. In the solid state physics the relation is known as Heine equation [53].

The 3DSL model predicts the red shift $\Delta_n = E_n^{\mathrm{HAP}} - E^{\mathrm{bone}} \approx 2E_{\mathrm{n}}\frac{<\tilde{d}>}{<L>} > 0$ of valence bands in bone mineral compared to those, E_n^{HAP}, in HAP crystal and links the shift with super-long-order parameters of conglomerate and with peculiarities of electrons propagation through the conglomerate. $<\tilde{d}>$ and $<L>$ are respectively the electron-optical length of hydrated nanolayers and mean linear size of HAPN. As the potential $\varphi(r)$ is found varying substantially with age, an essential age dependence of the electron-optical length $<\tilde{d}>$ can be predicted. Therefore, the energy E^{bone} of valence bands in mineralized bone is expected to be age dependent characteristic of its electron structure.

Pay also attention that X-ray dichroism in photoemission from cortical bone [54] suggests a

dependence of charge transfer and quantum phenomena on the orientation of HAPN relative to the principal axes of bone. As, according to the Wolf paradigm [55], the orientation of bone structures is determined by the locomotor functions of the body against gravity, it can be assumed that the quantization axes of bone nanostructures are directly connected with directions of gravitational forces in the skeleton. This means, when studying biomineralization mechanisms, quantum effects should be considered as related to the direction of gravity. Thus, quantum phenomena are expected to play an important role in bone tissues, in particular, when molecular signals propagate along them [56]. These phenomena require further detailed research, so we will not discuss them in more detail here.

The built-in charge Q and the energy $\mathscr{E}$ are determined not only by Ca^{2+} vacancies, calcium deficiency, and geometry of HAPN, but also by substitutions at all crystallographic positions, which affect the charge. Thus, for instance, the substitution of Ca^{2+} for Na_{+} and OH^{-} for O^{2-} increases Q, while carbonation, conversely, leads to its decrease. The impact of such substitutions, which may be motivated by environmental and nutritional factors, was not considered here too. Further research is needed to study their impact on the electrophysical properties of bone, as well as further quantitative testing of the BB concept.

5. Conclusion

Significant influence of the electrostatic fields generated by built-in charges in HAPNs on the atomic structure and dynamics of native bone has been revealed. In young bone, a potential difference is expected between the negatively charged surfaces of bioapatite nanocrystals and the positively charged hydrated nanolayers. In mature bone both the difference $\Delta\varphi$ and the electric field strength F are reduced approximately by 10 times.

The experimental data analysis revealed a specific two-component layout of $\nu_1[PO_4]^{3-}$-band, which is caused by the different effects of electrostatic fields in the bulk and at the interface of HAPN. The bulk component demonstrates a predominant Gaussian shape whereas the interface component appears as a distinct Lorentzian. This difference is attributed to the strong polarization and ordering of phosphate ions on the interface due to the internal fields in bone. The study confirms the BB concept and makes evident an important role of intrinsic electrostatic interactions in mineralized bone. We speculate that early-formed dipoles may retain their orientation during later growth, which could explain the observed trend.

The obtained results allow us to predict the specific quantization of electronic states in the mineral matrix and the alignment of the quantization axes along the directions of gravitational forces the skeleton.

Finalizing, this work may guide (i) design of bio-inspired energy materials, (ii) new strategies for targeted drug delivery based on bone charge, and (iii) development of electrophysical tools for bone health monitoring.

List of abbreviations

HAP - hydroxyapatite;

HAPN - hydroxyapatite nanocrystal;

BB - bone battery;

DEL - double electric layer;

BE - binding energy

XRD - X-ray diffraction

XPS - X-ray Photoelectron Spectroscopy

NMR – Nuclear Magnetic Resonance

Author Contributions

Andery Pavlychev: conceptualization, supervision, methodology, validation, funding acquisition, visualization, formal analysis, writing; Xenia Brykalova: software, resources, formal analysis, visualization, methodology, data curation: Aleksei Konachuk: resources, measurements, methodology, software, validation, for-mal analysis, data curation, writing; Alexandr Cherny: resources, methodology, formal analysis, samples, data curation, writing; Anatoliy Korneev resources, validation, methodology, formal analysis, data curation. All co-authors participated in the discussion of the study results. All authors have read and agreed to the published version of the manuscript.

Availability of Data and Materials

The data are available upon contacting the resource centers (https://researchpar.spbu.ru and https://client/researchpark.ru) of the Science Park of St. Petersburg State University.

Ethical Committee Approval:

The study protocol 10-10-2015 was approved after reviewing by Local Ethic Committee of R.R. Vreden National Medical Research Centre of Traumatology and Orthopaedics.

Animals Rights Statement:
All experimental procedures involving animals were performed following the ARRIVE guidelines. The research complies with all applicable national laws (GOST R ISO 10993-2-2009 — medical devices, biological evaluation of medical devices; part2, animal welfare requirements), regulations and guidelines in accordance with ISO 10993 that ensures the high animal welfare standards, as well as national regulations rules GOST 33215-2014 and GOST 33216-2014 — rules for the maintenance and care of laboratory rodents and rabbits. All animals were kept under identical conditions in the vivarium of the National Medical Research Center of Traumatology and Orthopedics.

Conflict of Interest

The authors declare no conflicts of interest in the current study.

Funding

This work is financially supported by Russian Science Foundation Grant 23-21-00172.

Acknowledgments

This research was carried out with the technical support of the Centre for Physical Methods of Surface Investigation, Centre for Diagnostics of Functional Materials for Medicine, Pharmacology and Nanoelectronics and Centre for Optical and Laser Methods for Studying Matter at St. Petersburg State University.

AI-declaration: The authors confirm that no artificial intelligence tools were used in the writing and preparation of this article.

References

1. Jun Guo, Feng Gao, Feng Zhang, Xinmin Zhao, and Ruoyang Zhao Biomineralization-Driven Advances in Materials Science and Biomedical Engineering. JACS Au, 2025, 5, 4134−4154

2. Gilbert PUPA, Bergmann KD, Boekelheide N, Tambutté S, Mass T, Marin F, Adkins JF, Erez J, Gilbert B, Knutson V, Cantine M, Hernández JO, Knoll AH. Biomineralization: Integrating mechanism and evolutionary history. Sci Adv. 2022;8(10):eabl9653.

3. Yan X, Zhang Q, Ma X, Zhong Y, Tang H, Mai S. The mechanism of biomineralization: Progress in mineralization from intracellular generation to extracellular deposition. Jpn Dent Sci Rev. 2023;59,181-190.

4. Vernadsky VI. Biosphere. Scientific Chemical Technical Publishing House, Scientific and Technical Department. (Leningrad), 1926. -146 p.

5. Barinov SM. Calcium phosphate-based ceramic and composite materials for medicine. Russ.Chem.Rev. 2010,79 (1), 13–29.

6. Samoylov YB. Biolytes, Leningrad, Scientific Chemical Technical Publishing House, 1929. 140 p.

7. Iafisco M, Delgado-López JM. (Editors) Apatite: Synthesis, Structural Characterization and Biomedical Applications in Geology and Mineralogy Research Developments Materials Science and Technologies Series/Geology and mineralogy research developments Nova Science Publishers, 2014, 364 p.

8. Landis WJ, Hodgens KJ, Arena J, Song MJ, McEwen BF. Microscopy Res and Technique. 1996;33:192-202.

9. Lin K, Wu C, Chang, Advances in synthesis of calcium phosphate crystals with controlled size and shape J. Acta Biomater. 2014;10:4071–4102.

10. Denisov-Nikolski YuI, Mironov SP, Omeljanenko NP. Actual problems of theoretical and clinical osteoartrology. M. JSC Printing-house “News; 2005, 336 p.

11. Avrunin AS, Tikhilov RM, Abolin AB, Shcherback IG. Morphology [Morfologiia], 2005, 2,78-82.[in Rus.]

12. Yao S, Jin B, Liu Z, Shao C, Zhao R, Wang X, and Tang R. Biomineralization: From Material Tactics to Biological Strategy, Adv. Mater. 2017; 29, 1605903.

13. Cuéllar-Cruz M. Synthesis of inorganic and organic crystals mediated by proteins in different biological organisms. A mechanism of biomineralization conserved throughout evolution in all living species, Prog. Cryst. Growth Charact. Mater., 2017, 63, 94–103

14. Engel J. A Critical Survey of Biomineralization. Control, Mechanisms, Functions and Material Properties. Springer Briefs in Appl. Sci. Tech., Springer International Publishing, 2017, 64 p

15. Deymier AC, Nair AK, Depalle B, Qin Z, Arcot K, Drouet C, Yoder CH, Buehler MJ, Thomopoulos S, Genin G, Pasteris M, Jill D. Protein-free formation of bone-like apatite: New insights into the key role of carbonation. Biomaterials, 2017, 127, 75-88.

16. Lotsari A, Rajasekharan AK, Halvarsson M, Andersson M. Transformation of amorphous calcium phosphate to bone-like apatite. Nat Commun. 2018;9(1):4170.

17. Brykalova XO, Kornilov NN and Pavlychev AA, The peculiarities of charge distribution and spatiotemporal changes in electronic and atomic structure of bone tissue, J. Mater. Chem. A, 2022; 10, 22686-22693

18. Wopenka B., Pasteris J.D. A mineralogical perspective on the apatite in bone. Mater Sci & Eng: C, 2005, 25(2):131-143.

19. Yadi Sun, Yan Wang, Chunhui Ji, Jianxiong Ma, Bingnan He Sci Rep, The impact of hydroxyapatite crystal structures and protein interactions on bone's mechanical properties. 2024;14:9786.

20. PavlychevAA, Brykalova XO, Cherny AA, Korneev AV and Kornilov NN, Spatiotemporal Changes in Atomic and Molecular Architecture of Mineralized Bone under Pathogenic Conditions, Crystals, 2023, 13(3), 381.

21. Avrunin AS. et al., Influence of the Skeleton Hierarchical Organization on Electronic State of Ions in Bone Matrix. Traumatology and Orthopedics, 2016; 22(4), 88-97.

22. Frank-Kamenetskaya O, Kol'tsov A, Kuz'mina M, Zorina M, Poritskaya L. Ion substitutions and non-stoichiometry of carbonated apatite-(CaOH) synthesised by precipitation and hydrothermal methods. J. Mol. Struct., 2011; 992, 9-18

23. Yifei Xu Johanna M. Galloway, L. Jorin Hasselt, and Fiona C. The Role of Confinement in Biomineralization Meldrum. Chem. Rev. 2025, 125, 12128−12197

24. Mandair GS, Morris MD, Contributions of Raman spectroscopy to the understanding of bone strength, BoneKey Reports, 2015; 4, 620;

25. Penel G, Delfosse C, Descamps M, Leroy G, Composition of bone and apatitic biomaterials as revealed by intravital Raman microspectroscopy, Bone, 2005, 36, 893-901;

26. Gouadec G, Colomban P, Raman Spectroscopy of nanomaterials: How spectra relate to disorder, particle size and mechanical properties. Prog. Cryst. Growth Charact Mater., Elsevier, 2007, 53, 1-56.

27. Pavlychev AA, Brykalova XO, Korneev AV, Cherny AA, and Kornilov NN, Specific Features of the Crystal Structure of Calcium Hydroxyapatite in Native Bone Tissue, Crystallography Reports, 2024, 69(1), 38-44

28. Frank-Kamenetskaya OV, Vlasov DYu, Panova EG, Lessovaia SN, (Eds) In: Processes and Phenomena on the Boundary Between Biogenic and Abiogenic Nature; Lecture Notes in Earth System Sciences (book series), Springer Cham, 2020; ISSN 2193-858X.

29. Colomban Ph, Sagon G, and Faurel X, Differentiation of Antique Ceramics from the Raman Spectra of their Colored Glazes and Paintings, J. Raman Spectrosc. 2001, 32, 351;

30. Gouadec G, Colomban Ph, and Bansal NP, Raman Study of Hi-Nicalon Fiber Reinforced Celsian Composites, Part1: Distribution and Nanostructure of Different Phases, J. Am. Ceram. Soc. 2001; 84, 1129.

31. Colomban Ph, Gouadec G, and Mazerolles L, Raman Analysis of Materials Corrosion: the Example of SiC Fibers, Materials and Corrosion. 2002; 53, 306.

32. Cabot A, Diéguez A, Romano-Rodriguez A, Morante JR and Barsan N, Influence of the Catalytic Introduction Procedure on the Nano-SnO2 Gas Sensor Performances. Where and How Stay the Catalytic Atoms ?, Sens. Actuators B, 2001; 79, 98.

33. Cassoux P, de-Caro D, Valade L, Casellas H, Roques S, and Legros J-P, Thin Films and Nanowires of Molecule-Based Conductors and Magnets, Synthetic Met, 2003, 133-134, 659.

34. Fang GJ, Yao K-L, and Liu Z-L, Fabrication and Electrochromic Properties of Double Layer WO3(V)/V2O5(Ti) Thin Films Prepared by Pulsed Laser Ablation Technique, Thin Solid Films, 2001, 394, 64.

35. Poborchii VV, Raman Spectra of Sulfur, Selenium or Tellurium Clusters Confined in Nano-Cavities of Zeolite A, Solid State Comm. 1998,107, 513.

36. Rodríguez-Cabello JC, Quintanilla L, Pastor JM, Fourier Transform Raman Study of the Conformers in Poly(ethylene terephtalate), J. Raman Spectrosc. 1994, 25, 335.

37. Li X, Chen W, Bian C, He J, Xu N, Xue G, Surface Modification of TiO2 NanoParticles by Polyaniline, Appl. Surf. Sci. 2003, 217, 16.

38. Pavlychev A, Brykalova X, Cherny A, Konashuk A, Korneev A, In: Mechanical Loads and Site-Dependent Changes in Crystal Structure and Molecular Dynamics in Native Bone. Springer Series Book *Machine and Materials Science* vol.156, Chapter 33. Xiaowei Yue and Kunjie Yuan (Eds.): Proceedings the 6th Int. Conf. Mechanical Engineering and Applied Composite Materials; 2023.

39. Aggarwal RL; Farrar LW; Greeneltch NG. et al. Measurement of the Raman Line Widths of Neat Benzenethiol and a Self-Assembled Monolayer (SAM) of Benzenethiol on a Silver-Coated Surface-Enhanced Raman Scattering (SERS) Substrate, Appl. Spectrosc., 2012, 66(7), 740-743.

40. Tu Z, Achazi K, Schulz A, Mülhaupt R, Thierbach S, Rühl E, Adeli M, Haag R. Combination of Surface Charge and Size Controls the Cellular Uptake of Functionalized Graphene Sheets, Adv. Funct. Mater. 2017, 27(33), 1701837

41. Wilson EE, Awonusi A, Morris MD et al. Highly ordered interstitial water observed in bone by nuclear magnetic resonance. J Bone Min. Res. 2005, 20(4), 625-634.

42. Zakharov NA and Orlovsky VP, Dielectric characteristics of biocompatible $Ca_{10}(PO_4)_6(OH)_2$ ceramics, Tech. Phys. Lett. 2001, 27, 629–631

43. Qi C, Zhu Z, Wang C, Zheng Y, Anomalously Low Dielectric Constant of Ordered Interfacial Water, J. Phys. Chem. Lett. 2021; 12, 931–937

44. Olivieri F, Hynes JT, Laage D, Confined Water's Dielectric Constant Reduction Is Due to the Surrounding Low Dielectric Media and Not to Interfacial Molecular Ordering, J. Phys. Chem. Lett. 2021; 12, 4319–4326.

45. Zhang Y, de Aguiar HB, Hynes JT, Laage D, Water Structure, Dynamics, and Sum-Frequency Generation Spectra at Electrified Graphene Interfaces, J. Phys. Chem. Lett. 2020; 11, 624–631.

46. S. V. Dorozhkin, Amorphous Calcium Orthophosphates: Nature, Chemistry and Biomedical Applications, Int. J Mater. Chem. 2012, 2(1), 19-46

47. Wehrmeister U, Jacob D. E. Soldati AL, Loges N, Häger T, Hofmeister W, Amorphous, nanocrystalline and crystalline calcium carbonates in biological materials, J. Raman spectrosc., 2010; 42(5), 926-935

48. Katsikini M, Proiou E, Vouroutzis N, Pinakidou F, Paloura EC, Smirnov D, Brzhezinskaya M, Ves S, Crystalline and amorphous calcium carbonate as structural components of the *Calappa granulata* exoskeleton, J. Struct. Biology, 2020, 211(3), 107557.

49. Jacob DE, Wirth R, Soldati AL, Wehrmeister U, Schreiber A, Amorphous calcium carbonate in the shells of adult Unionoida, J. Struct. Biol. 2011, 173(2): 241-9.

50. Combes C, Rey C, Amorphous calcium phosphates: synthesis, properties and uses in biomaterials. Acta Biomaterialia, 2010; 6(9), 3362-3378.

51. Demnati I, Grossin D, Marsan O, Bertrand G, Collonges G, Combes C, Parco M, Braceras I, Alexis J, Balcaen Y, Christian Rey C, Comparison of Physical-chemical and Mechanical Properties of Chlorapatite and Hydroxyapatite Plasma Sprayed Coatings, The Open Biomed. Engin. J., 2015, 9, (Suppl 1-M3), 42-55

52. Pavlychev AA; Avrunin AS; Vinogradov AS; Filatova EO; Doctorov AA; Krivosenko YS; Samoilenko DO; Svirskiy GI; Konashuk AS; Rostov DA, Local electronic structure and nanolevel hierarchical organization of bone tissue: Theory and NEXAFS study. Nanotech., 2016, 27, 504002.

53. Heine V, Solid State Physics. Adv. Res. Appl., 1970; 24, 1-36

54. Konashuk AS, Brykalova XO, Kornilov NN, Filatova EO, Pavlychev AA, Hierarchy-induced X-ray Linear Dichroism in Cortical Bone, Emerg. Mater., 2020; 3(4), 515-520.

55. Wolff J, Das Gesetz der Transformation der Knochen; Hirschwald: Berlin, 1892.

56. Shah HN, Amanatullah DF, Longaker MT, Lowenberg DW, Bridging technique and science: A review of the molecular signals from long bone development that guiding bone regeneration, Orthoplastic Surgery, 2022, 9(9), 86-92.